Short-lag spatial coherence beamforming of photoacoustic images for enhanced visualization of prostate brachytherapy seeds

Muyinatu A. Lediju Bell,[1,2]* **Nathanael Kuo,**[3] **Danny Y. Song,**[4] **and Emad M. Boctor**[1,2]

[1]*Department of Computer Science, Johns Hopkins University, Baltimore, MD, 21218, USA*
[2]*Department of Radiology and Radiological Sciences, Johns Hopkins University School of Medicine, Baltimore, MD, 21213, USA*
[3]*Department of Biomedical Engineering, Johns Hopkins University, Baltimore, MD, 21218, USA*
[4]*Department of Radiation Oncology and Molecular Radiation Sciences, Johns Hopkins University School of Medicine, Baltimore, MD, 21213, USA*

[*]muyinatu.ledijubell@jhu.edu

Abstract: Prostate brachytherapy, administered by implanting tiny radioactive seeds to treat prostate cancer, currently relies on transrectal ultrasound imaging for intraoperative visualization of the metallic seeds. Photoacoustic (PA) imaging has been suggested as a feasible alternative to ultrasound imaging due to its superior sensitivity to metal surrounded by tissue. However, PA images suffer from poor contrast when seeds are distant from the light source. We propose a transperineal light delivery method and investigate the application of a short-lag spatial coherence (SLSC) beamformer to enhance low-contrast photoacoustic signals that are distant from this type of light source. Performance is compared to a conventional delay-and-sum beamformer. A pure gelatin phantom was implanted with black ink-coated brachytherapy seeds and the mean contrast was improved by 3-25 dB with the SLSC beamformer for fiber-seed distances ranging 0.6-6.3 cm, when approximately 10% of the receive aperture elements were included in the short-lag sum. For fiber-seed distances greater than 3-4 cm, the mean contrast-to-noise ratio (CNR) was approximately doubled with the SLSC beamformer, while mean signal-to-noise ratios (SNR) were mostly similar with both beamformers. Lateral resolution was decreased by 2 mm, but improved with larger short-lag values at the expense of poorer CNR and SNR. Similar contrast and CNR improvements were achieved with an uncoated brachytherapy seed implanted in *ex vivo* tissue. Results indicate that the SLSC beamformer has potential to enhance the visualization of prostate brachytherapy seeds that are distant from the light source.

© 2013 Optical Society of America

References and links

1. S. Langley and R. Laing, "Prostate brachytherapy has come of age: a review of the technique and results," Brit. J. Urol. **89**, 241–249 (2002).
2. N. Kuo, H. J. Kang, D. Y. Song, J. U. Kang, and E. M. Boctor, "Real-time photoacoustic imaging of prostate brachytherapy seeds using a clinical ultrasound system," J. Biomed. Opt. **17**, 0660051–0660057 (2012).
3. T. Harrison and R. J. Zemp, "Coregistered photoacoustic-ultrasound imaging applied to brachytherapy," J. Biomed. Opt. **16**, 080502–080502 (2011).
4. J. L. Su, R. R. Bouchard, A. B. Karpiouk, J. D. Hazle, and S. Y. Emelianov, "Photoacoustic imaging of prostate brachytherapy seeds," Biomed. Opt. Express **2**, 2243 (2011).
5. A. G. Bell, "On the production and reproduction of sound by light", Am. J. Sci. **118**, 305–324 (1880).
6. M. Xu and L. V. Wang, "Photoacoustic imaging in biomedicine," Rev. Sci. Instrum. **77**, 041101–041101 (2006).
7. E. M. Boctor, "Prostate brachytherapy seed localization using combined photoacoustic and ultrasound imaging," presented at SPIE Ultrasonic Imaging, Tomography and Therapy, San Diego, California, 14 Feb. 2010.
8. N. Kuo, H. J. Kang, T. DeJournett, J. Spicer, and E. Boctor, "Photoacoustic imaging of prostate brachytherapy seeds in ex vivo prostate," Proc. SPIE 796409 (2011).
9. L. Pan, A. Baghani, R. Rohling, P. Abolmaesumi, S. Salcudean, and S. Tang, "Improving photoacoustic imaging contrast of brachytherapy seeds," Proc. SPIE 85814B (2013).
10. T. Mitcham, K. Homan, W. Frey, Y.-S. Chen, S. Emelianov, J. Hazle, and R. Bouchard, "Modulation of photoacoustic signal generation from metallic surfaces," J. Biomed. Opt. **18**, 056008 (2013).
11. M. Jaeger, S. Schüpbach, A. Gertsch, M. Kitz, and M. Frenz, "Fourier reconstruction in optoacoustic imaging using truncated regularized inverse k-space interpolation," Inverse Probl. **23**, S51 (2007).
12. B. E. Treeby and B. T. Cox, "k-Wave: MATLAB toolbox for the simulation and reconstruction of photoacoustic wave fields," J. Biomed. Opt. **15**, 021314 (2010).
13. S. Park, A. B. Karpiouk, S. R. Aglyamov, and S. Y. Emelianov, "Adaptive beamforming for photoacoustic imaging," Opt. Lett. **33**, 1291–1293 (2008).
14. M. A. Lediju, G. E. Trahey, B. C. Byram, and J. J. Dahl, "Short-lag spatial coherence of backscattered echoes: Imaging characteristics," IEEE Trans. Ultrason. Ferr. Freq. Contr. **58**, 1337 (2011).
15. J. J. Dahl, D. Hyun, M. A. Lediju, and G. E. Trahey, "Lesion detectability in diagnostic ultrasound with short-lag spatial coherence imaging." Ultrasonic Imaging **33**, 119 (2011).
16. M. A. Lediju Bell, R. Goswami, and G. E. Trahey, "Clutter reduction in echocardiography with short-lag spatial coherence (SLSC) imaging," in *Proceedings of IEEE International Symposium on Biomedical Imaging* (IEEE, 2012), pp. 1116–1119.
17. M. A. Lediju Bell, R. Goswami, J. A. Kisslo, J. J. Dahl, and G. E. Trahey, "Short-lag spatial coherence imaging of cardiac ultrasound data: Initial clinical results," Ultrasound Med. Biol. **39**(10), 1861–1874 (2013).
18. M. A. Lediju Bell, R. Goswami, J. J. Dahl, and G. E. Trahey, "Improved visualization of endocardial borders with short-lag spatial coherence imaging of fundamental and harmonic ultrasound data," in *Proceedings of IEEE International Ultrasonics Symposium* (IEEE, 2012), pp. 2129–2132.
19. M. Jakovljevic, G. E. Trahey, R. C. Nelson, and J. J. Dahl, "*In Vivo* application of short-lag spatial coherence imaging in human liver," Ultrasound Med. Biol. **39**, 534–542 (2013).
20. B. Pourebrahimi, S. Yoon, D. Dopsa, and M. C. Kolios, "Improving the quality of photoacoustic images using the short-lag spatial coherence imaging technique," Proc. SPIE 85813Y (2013)
21. C. G. Roehrborn, C. J. Girman, T. Rhodes, K. A. Hanson, G. N. Collins, S. M. Sech, S. J. Jacobsen, W. M. Garraway, and M. M. Lieber, "Correlation between prostate size estimated by digital rectal examination and measured by transrectal ultrasound," Urology **49**, 548–557 (1997).
22. A. Standard, "Z136. 1. American national standard for the safe use of lasers. American National Standards Institute," Inc., New York (1993).
23. W. H. Nau, R. J. Roselli, and D. F. Milam, "Measurement of thermal effects on the optical properties of prostate tissue at wavelengths of 1,064 and 633 nm," Laser. Surg. Med. **24**, 38–47 (1999).
24. J. L. Karagiannes, Z. Zhang, B. Grossweiner, and L. I. Grossweiner, "Applications of the 1-D diffusion approximation to the optics of tissues and tissue phantoms," Appl. Optics **28**, 2311–2317 (1989).
25. W.-F. Cheong, S. A. Prahl, and A. J. Welch, "A review of the optical properties of biological tissues," IEEE J. Quantum Elect. **26**, 2166–2185 (1990).
26. R. J. Fedewa, K. D. Wallace, M. R. Holland, J. R. Jago, G. C. Ng, M. R. Rielly, B. S. Robinson, and J. G. Miller, "Spatial coherence of the nonlinearly generated second harmonic portion of backscatter for a clinical imaging system," IEEE Trans. Ultrason. Ferr. Freq. Contr. **50**, 1010–1022 (2003).
27. R. Mallart and M. Fink, "The van Cittert–Zernike theorem in pulse echo measurements," J. Acoust. Soc. Am. **90**, 2718 (1991).

1. Introduction

Brachytherapy is a localized form of radiation therapy that is administered by implanting small, metallic, radioactive seeds in the organ being treated. Prostate brachytherapy seeds are currently visualized with transrectal ultrasound (TRUS) imaging during implantation, but they are sometimes difficult to locate due to factors like their small size and their poor acoustic contrast with surrounding tissue [1]. Photoacoustic (PA) imaging is currently being investigated as a feasible alternative to ultrasound imaging for intraoperative localization of prostate brachytherapy seeds [2–4]. Implemented by delivering nanosecond light pulses to the prostate, photoacoustic imaging is advantageous because the optical absorption difference between metal and tissue is larger than the corresponding acoustic impedance differences. Optical absorption causes thermoelastic expansion and the subsequent generation of broadband sound waves, which are detectable with an ultrasound transducer [5, 6]. Therefore, a light delivery system is the only additional equipment required to introduce photoacoustic imaging into the current workflow of brachytherapy procedures.

Several researchers previously investigated the feasibility of visualizing prostate brachytherapy seeds with photoacoustic imaging [2–4, 7]. Harrison and Zemp [3] demonstrated that brachytherapy seeds were distinguishable from a blood-filled tube and surrounding *ex vivo* tissue using a laser wavelength of 1064 nm. Su et al. [4] and Kuo et al. [2, 8] demonstrated the dependence of photoacoustic signal amplitude on seed orientation relative to the ultrasound transducer. In addition, Kuo et al. [2] describe a real-time clinical system prototype for photoacoustic imaging of prostate brachytherapy seeds.

One outstanding challenge to brachytherapy seed visualization with PA imaging is the suboptimal visibility with increasing distance from the light source (i.e. when seeds are not exposed to sufficient laser fluence) [4]. To increase image contrast, Pan et al. [9] demonstrated that brachytherapy seeds may be coated with an optically absorbing material. In addition, Mitcham et al. [10] demonstrated that increasing metal surface roughness increases optical absorption, which has promise for increasing the contrast of the metallic brachytherapy seeds in photoacoustic images. Both approaches require alterations to the brachytherapy seeds.

An alternative approach is to consider the beamforming of photoacoustic data. Conventional photoacoustic beamformers display the amplitude of received signals, with the delay-and-sum beamformer being one of the most common. Another common beamforming approach utilizes the Fourier transform of received photoacoustic signals [11, 12]. A minimum variance adaptive beamformer has also been investigated [13]. While advantages of these beamformers include reduced clutter noise artifacts and improved resolution, they primarily depend on signal amplitude, and thus suffer from diminishing PA image contrast with decreasing light fluence.

The short-lag spatial coherence (SLSC) beamformer has potential to overcome the PA signal dependency on distance from the light source, as calculations of spatial coherence are independent of signal amplitude. This beamformer calculates the spatial coherence of signals received by closely-spaced transducer elements and displays the information as an image [14]. SLSC imaging improved lesion detectability in the presence of acoustic noise artifacts, when compared to conventional B-mode ultrasound imaging [15]. In addition, this beamformer was applied to *in vivo* ultrasound data to reduce clutter noise artifacts in cardiac [16–18], liver [19], thyroid [14], and vascular [15] images. Similar clutter reduction benefits were achieved when the SLSC beamformer was applied to photoacoustic data [20].

This paper evaluates the performance of the SLSC beamformer for photoacoustic imaging of prostate brachytherapy seeds. Utilizing a transrectal ultrasound probe and an optical fiber, we present phantom and *ex vivo* validation experiments. In addition, we introduce a transperineal interstitial light delivery approach for photoacoustic imaging of prostate brachytherapy seeds. In a potential clinical scenario with transperineal insertion of brachytherapy seeds and the opti-
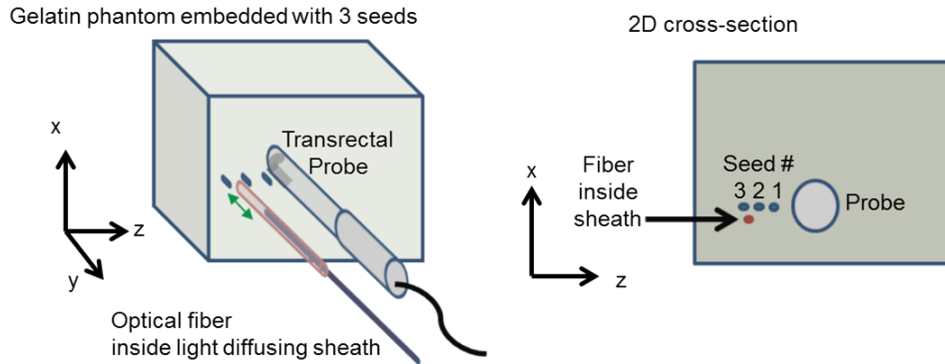
Fig. 1. A gelatin phantom was implanted with coated brachytherapy seeds separated by 5 mm in the z direction. An optical fiber was inserted into a light diffusing sheath and placed approximately 6 mm below the y-z plane of the seeds. The fiber-sheath tip distance, indicated by the green double arrow, was varied from 0 cm to 5 cm. The 2-D cross-section view shows the orientation of the seeds relative to the fiber, with seed # 1 being closest to the probe and farthest from the fiber.

cal fiber, the fiber's distance from the seeds may vary in the longitudinal direction of the TRUS probe. Measured prostate sizes range 1.4 - 8.7 cm in this direction, with means ranging 3.8 - 4.6 cm [21].

2. Methods and materials

2.1. Phantom experiments

A phantom consisting of 10% porcine skin gelatin (Type A, Sigma-Aldrich Co., St. Louis, MO) and 90% water was drilled with a cylindrical tube to accommodate the insertion of a TRUS probe. Optical or acoustic scatterers were not included in the phantom to create an ideal environment for evaluating the DAS beamformer. Non-radioactive, titanium, cylindrical brachytherapy seeds (TheraSeed, Theragenics Corporation, Buford, GA, USA) of length of 4.5 mm and outer diameter 0.8 mm were painted with black India ink to increase optical absorption. This black coating was achieved by immersing the seeds in the India ink and allowing them to air dry before applying another coat of ink. At least three coats of ink were applied to each seed. This coating increased the diameter of the seeds by less than 0.1 mm.

Utilizing a standard 18G hollow brachytherapy needle and needle template grid, the coated seeds were deposited at a distance of 5 cm from the needle insertion point on the face of the phantom, and the spacing between the seeds was approximately 5 mm in the z-direction of Fig. 1. This spacing corresponded with the minimum distance between the holes in the brachytherapy needle template grid. For reference purposes, the seeds were numbered as shown in the 2D cross-section view of Fig. 1, with seed #1 being closest to the probe, at a distance of approximately 12 mm from the cylindrical channel created for the TRUS probe.

The light source was a Brilliant (360 mJ) neodymium-doped yttrium aluminum garnet (Nd:YAG) laser manufactured by Quantel (Bozeman, MT) with an optical parametric oscillator installed by Opotek (Carlsbad, CA). The laser repetition rate was 10 Hz, and the pulse duration was 5 ns. The laser was operated at 1064 nm wavelength to acquire photoacoustic images.

The free space laser beam was coupled to a 1 mm core diameter optical fiber with a 0.37 numerical aperture (Newport F-MBE, Irvine, CA). The free end of the fiber was inserted into a

hollow, plastic, high-dose-rate (HDR) brachytherapy needle of inner diameter 1.5 mm and outer diameter 2.0 mm (ProGuide 6F sharp, manufactured by Nucletron, Veenendaal, The Netherlands). This HDR brachytherapy needle acted as a light-diffusing sheath that enabled radial light delivery to the seeds, with the light distributed within a 2-cm radius surrounding the tip of the fiber. The radial light distribution due to the sheath was confirmed by coupling visible laser light (635 nm) to the fiber and observing the beam pattern in air before and after the free end of the fiber was inserted into the sheath. The average energy per pulse delivered through the pointed, conical tip of the sheath was approximately 11.2 mJ, which corresponds with an energy density of 178 mJ/cm^2 when calculated from measurements of the cone slant height (2 mm) and base diameter (2 mm). The energy density exceeded ANSI limits for human exposure (i.e. 100 mJ/cm^2 with a laser wavelength of 1064 nm) [22] to facilitate comparisons based on idealistic energy parameters.

The fiber, surrounded by the light diffusing sheath, was inserted in the gelatin phantom parallel to the long axes of the seeds, as shown in Fig. 1. The distances between the fiber and seeds #1, 2, and 3 were approximately 8, 6, and 8 mm, respectively, in the x-direction and 11, 4, and 2 mm, respectively, in the z-direction, as measured in an ultrasound image. Although a grid was used to place the seeds along the same line, the x-coordinates of the three seeds are not the same due to a slight bending of the needle during insertion. The 2D distances between the fiber and seeds #1, 2, and 3 were 12.8, 8.7, and 6.5 mm, respectively, as measured in an ultrasound image. The optical fiber was gently pushed into the sheath until there was resistance from the tip of the sheath, confirming a distance of 0 cm between the fiber and sheath tips. This fiber-sheath tip distance was then varied from 0 cm to 5 cm, by 1 cm increments, as illustrated by the green double arrow in Fig. 1. This varied distance corresponds with average prostate sizes along the probe's longitudinal direction [21].

Based on Fig. 1, when the fiber-sheath tip distance is large (i.e. greater 2 cm), the light irradiating the seeds appears to travel along the length of the fiber and sheath, rather than radially. However, the light is spherically diffused around the location of the tip of the fiber inside the sheath in these cases. In addition, the conical tip of the sheath assists with radial light delivery at these larger distances, within a radius of at least 3 mm surrounding the tip of the sheath. These illumination profiles were confirmed by coupling 635 nm laser light to the fiber inside the sheath and observing the beam pattern in air with the fiber located at distances of 1-5 cm from the sheath tip.

An Ultrasonix (Richmond, BC, Canada) transrectal bi-plane ultrasound probe was inserted parallel to the optical fiber, as shown in Fig. 1, and used to acquire beamformed radiofrequency (RF) pulse-echo ultrasound data and pre-beamformed photoacoustic data. The transmit frequency for pulse-echo ultrasound was 9 MHz. Ultrasound and photoacoustic data were col-
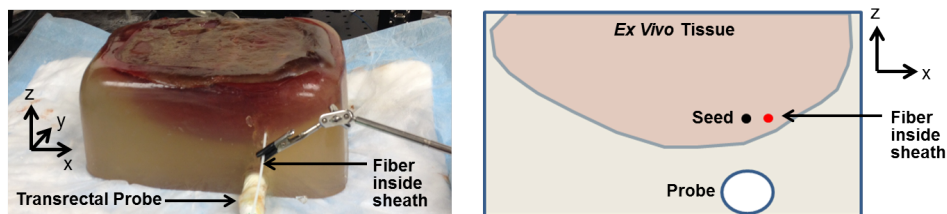

Fig. 2. An *ex vivo* bovine liver was embedded in gelatin and implanted with one non-radioactive, uncoated brachytherapy seed. The 2D cross-section view shows the orientation of the transrectal probe relative to the optical fiber and light diffusing sheath. The linear array is parallel to the y axis.

lected with the probe's linear (BPL9-5/55) and curvilinear (BPC8-4/10) arrays, which have center frequencies of 7 MHz and 6 MHz, respectively, and contain 128 elements each. An Ultrasonix SonixTouch ultrasound scanner was connected to the laser with a BNC cable. The three probe ports of the SonixTouch were occupied with the linear and curvilinear arrays of the TRUS probe and an Ultrasonix data acquisition (SonixDAQ) device. A trigger signal following each laser pulse was sent from the laser to the SonixDAQ for synchronized laser light emission and data acquisition with either array of the TRUS probe. Five frames of PA data were recorded for each acquisition. The sampling frequency was 40 MHz.

2.2. Ex vivo demonstration

To evaluate beamforming performance in a tissue-like environment, an *ex vivo* bovine liver was embedded in gelatin and implanted with an uncoated (i.e. not dyed with ink), non-radioactive brachytherapy seed (see Fig. 2). The *ex vivo* liver is expected to have similar sound scattering properties to prostatic tissue, while the light scattering properties are an order of magnitude larger in bovine liver compared to human prostates at a laser wavelength of 1064 nm [23–25]. In addition, the *ex vivo* liver retains more blood content than an *ex vivo* prostate, making it more representative of the blood levels expected in an *in vivo* scenario.

The brachytherapy seed was inserted with a standard 18G brachytherapy needle under ultrasound guidance. A 1-mm optical fiber was placed inside the sheath and inserted parallel to the transrectal probe at a distance of approximately 6.34 mm from the seed, as measured in an ultrasound image acquired with the curvilinear array. The laser energy delivered through the tip of the light diffusing sheath was approximately 8.0 mJ, which corresponds with an energy density of 127 mJ/cm^2. Similar to the phantom experiments, the energy density exceeded ANSI limits for human exposure [22] to facilitate beamforming comparisons based on idealistic energy parameters. All other imaging parameters were the same as those used in the phantom experiments, and the same imaging system and data acquisition methods were used to acquire ultrasound and photoacoustic images for this *ex vivo* experiment.

2.3. Signal processing

A conventional delay-and-sum (DAS) beamformer and a coherence-based SLSC beamformer were applied to the received photoacoustic signals. Received signal time delays were calculated with 33-element subapertures for the DAS and SLSC photoacoustic images. Hanning apodization was applied to the delayed signals for DAS beamforming. No apodization was applied for SLSC beamforming.

SLSC photoacoustic images were calculated using the following equations [14, 26]:

$$\hat{R}(m) = \frac{1}{N-m} \sum_{i=1}^{N-m} \frac{\sum_{n=n_1}^{n_2} s_i(n) s_{i+m}(n)}{\sqrt{\sum_{n=n_1}^{n_2} s_i^2(n) \sum_{n=n_1}^{n_2} s_{i+m}^2(n)}} \tag{1}$$

$$R_{sl} = \sum_{m=1}^{M} \hat{R}(m) \tag{2}$$

where $\hat{R}$ represents the normalized spatial correlation of received signals, m is the distance (i.e. lag) between two elements of the receive aperture in units of number of elements, R_{sl} is the short-lag spatial coherence, N is the total number of elements in the receive aperture, $s_i(n)$ is the time-delayed, zero-mean signal received by the ith element, n is the sample depth in units of samples, and M is number of lags included in the short-lag sum. The value of n was equivalent to the smallest wavelength within the bandwidth of the linear array (i.e. 0.308 mm). Unless

otherwise stated, the value of M was set to 4, which corresponds to 12% of the number of elements in the receive aperture.

Beamformed ultrasound and PA data were envelope-detected, normalized to the brightest image pixel, log compressed, and displayed with 10-35 dB dynamic range. In addition, images acquired with the curvilinear array were scan converted. No frame averaging was applied to display images or calculate the beamformer performance metrics. All image processing was performed with MATLAB software (The MathWorks, Inc., Natick, MA).

2.4. Performance metrics

Contrast (C), contrast-to-noise ratios (CNR), and signal-to-noise ratios (SNR) of brachytherapy seeds in DAS and SLSC photoacoustic images were calculated using the following equations:

$$C = 20\log_{10}\left(\frac{S_i}{S_o}\right) \tag{3}$$

$$CNR = \frac{|S_i - S_o|}{\sigma_o} \tag{4}$$

$$SNR = \frac{S_i}{\sigma_o} \tag{5}$$

where S_i and S_o are the means of the image data within regions of interest (ROIs) located inside and outside of the brachytherapy seed, respectively, and σ_o is the standard deviation of the data within the ROI located outside of the seed. Rectangular ROIs surrounding the maximum signal from the seed were manually selected for each seed in each image evaluated, and a matching ROI at the same depth and with the same size was automatically created, starting at a fixed lateral position to the right of the seed. The fixed lateral position was the same in SLSC and DAS images. The average ROI size $\pm$ one standard deviation was 1.4 ± 0.5 mm (axial) x 3.2 ± 1.0 mm (lateral) in SLSC and DAS photoacoustic images. The average lateral distance between the right edge of the seed ROI and the left edge of the noise ROI (i.e. the ROI located outside of the seed) was 6 mm.

C, CNR, and SNR were measured as a function of the 3D fiber-seed distance and as a function of the short-lag value, M. The 3D fiber-seed distance was calculated by combining the (x, z) fiber-seed distances measured from ultrasound images with the varied fiber distance along the length of the TRUS probe (i.e. y dimension in Fig. 1). In addition, resolution was assessed as a function of the short-lag value, M, by measuring the full width at half maximum (FWHM) of the seed's PA signal in the lateral dimension of the curvilinear array.

3. Results

B-mode images of the three implanted brachytherapy seeds acquired with the curvilinear and linear arrays of the transrectal probe are displayed in Fig. 3(a) and 3(b), respectively. The imaging plane of the curvilinear array (i.e. transverse scan) shows the diameter of the seeds, while that of the linear array (i.e. longitudinal scan) shows the long axis of the seeds. The yellow arrows point to the location of the three seeds, and the red arrow points to the location of the fiber inside the light diffusing sheath. Air gaps created by the needle used to insert the seeds and previous fiber insertions are additionally visualized in the transverse and longitudinal ultrasound images. The fiber is not visualized in the longitudinal image because it is not in the imaging plane.

Photoacoustic images were overlaid on the B-mode images in a yellow-red color scale. Figures 3(c) and 3(d) respectively show the transverse and longitudinal PA images created with the DAS beamformer. Seeds #1 and 2 were difficult to visualize in the transverse image due
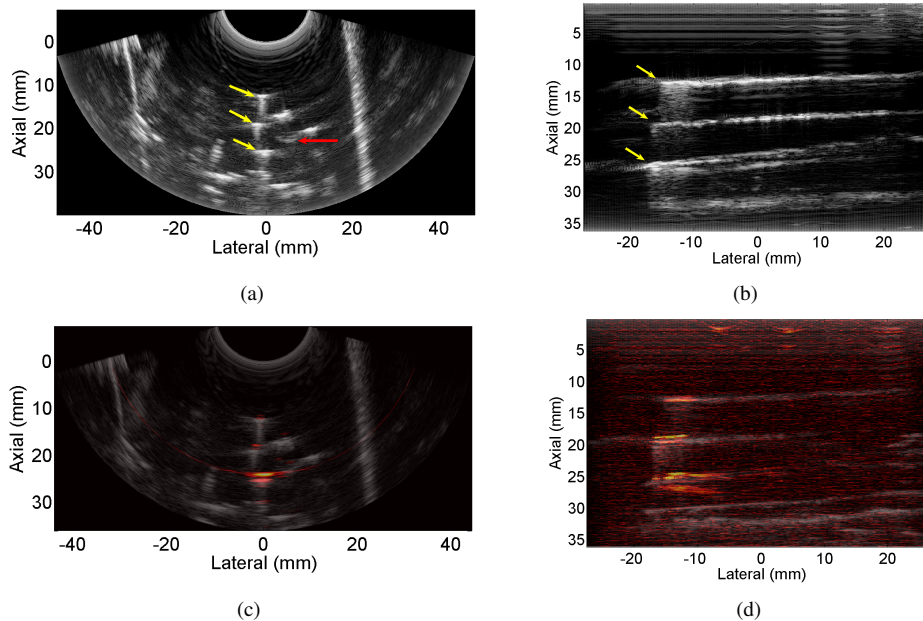
Fig. 3. B-mode ultrasound images acquired with (a) curvilinear and (b) linear arrays of the transrectal ultrasound probe. Yellow arrows point to the three implanted seeds, and the red arrow shows the location of the fiber. Seed #1 is the uppermost seed in each image. (c,d) Corresponding photoacoustic images overlaid on the B-mode images in a yellow-red color scale. The dynamic range of the B-mode images and the linear and curvilinear PA images was adjusted to 50, 35, and 20 dB, respectively.

to the low SNR of the PA signals. Visualization of the three seeds in the longitudinal image is similarly challenged by poor contrast and low SNR. The fiber-sheath distance was 0 cm and 3 cm, in Figs. 3(c) and 3(d), respectively.

Examples of the coherence curves used to form SLSC PA images are shown in Fig. 4. These curves were calculated using Eq. (1). The photoacoustic signals originating from brachytherapy seeds generally have higher spatial correlation than those originating from noise regions surrounding the seed. After summation of the short-lag values, as described by Eq. (2), PA signals originating from the seeds produce higher SLSC image pixel values relative to the noise regions surrounding them.

DAS and SLSC photoacoustic images are shown in Fig. 5 over the range of fiber-sheath distances investigated (i.e. 0-5 cm). As distance is increased, the background noise increases, particularly in the DAS images. The three seeds are more easily identified with the SLSC beamformer, particularly at larger distances from the primary light source (e.g. ≥ 2 cm). The SLSC images show less background noise when displayed with the same dynamic range as the DAS images. There is a fourth signal below seed #3 in the SLSC images that is particularly evident at fiber-sheath tip distances of 0 cm and 1 cm. This signal is due to the air gap created by a previous fiber insertion.

Performance metrics of the SLSC and DAS beamformers were measured for each of the three seeds, as a function of the 3D seed-fiber tip distance. Results were averaged over five image frames. Figure 6(a) reveals that the mean contrast obtained with the DAS beamformer decreases as distance from the fiber increases, while the mean contrast obtained with the SLSC
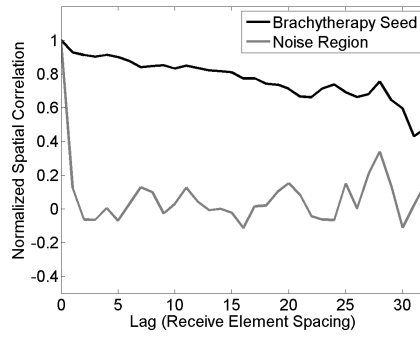
Fig. 4. Examples of the spatial coherence of time-delayed, photoacoustic wavefields originating from seed and noise regions, acquired with the curvilinear ultrasound array. Coherence curves like these were used to form SLSC photoacoustic images, as described by Eqs. (1) and (2).
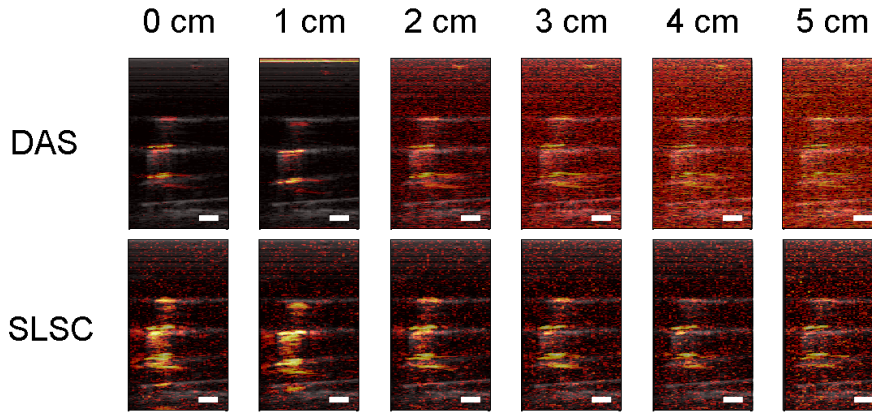

Fig. 5. DAS and SLSC photoacoustic images overlaid on B-mode images. The seeds were increasingly difficult to visualize with the DAS beamformer as distance from the light source increased. They were more easily visualized with the SLSC beamformer at the larger distances. Images are shown with 25 dB dynamic range. SLSC images were calculated with a short-lag value of M=4. The white bars, each 5 mm in length, denote the image scale. Seed #1 is the uppermost seed in each image.

beamformer is greater over the same range of distances. The mean contrast improvement ranged from 3-25 dB with the SLSC beamformer.

Although contrast is improved with the SLSC beamformer, Fig. 6(b) demonstrates that SNR with the SLSC beamformer was mostly similar at larger distances from the light source and degraded closer to the light source, when compared to SNR obtained with the DAS beamformer. The mean SNR difference between the two beamformers ranged from 0-16.

Figure 7 displays CNR as a function of the 3D distance between the fiber and seed. As shown in Fig. 7(a), the seed farthest from the light source (i.e. seed # 1), displays similar or at most a factor of 2.1 better CNR with the SLSC beamformer over the range of measured fiber-seed distances. For seeds #2-3, which are closer to the light source, the SLSC beamformer increases CNR by 1.4-3.1 compared to the DAS beamformer for fiber-seed distances greater than 3 cm. The DAS beamformer yields similar or at most a factor of 2.9 better CNR when the light source
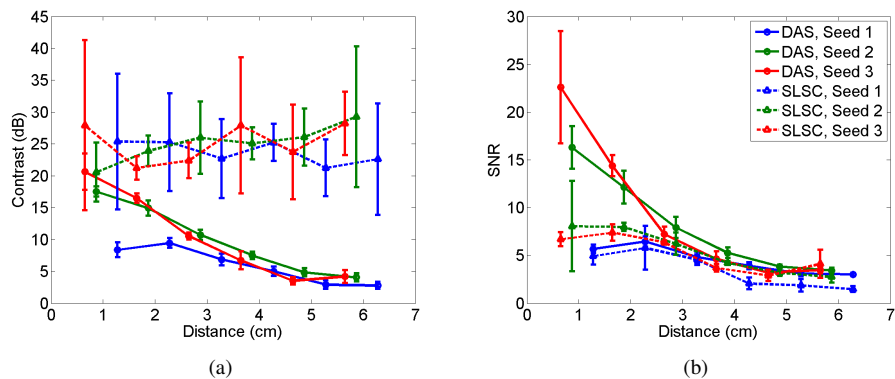
Fig. 6. (a) Contrast and (b) SNR as a function of distance between the seeds and optical fiber. Contrast is relatively constant with the SLSC beamformer, compared to the DAS beamformer. However, SNR with the SLSC beamformer ranges from similar to worse than SNR with the DAS beamformer. Error bars indicate $\pm$ one standard deviation of five image frames. SLSC performance metrics were calculated with a short-lag value of M=4.

is closer.

Examples of SLSC PA images created with different short-lag values (i.e. M) are shown in Fig. 8 along with corresponding DAS PA images. The transverse scans (top row) exhibit better visualization of seeds #1 and 2, which are poorly visualized with DAS beamforming. These seeds were farthest from the fiber. Note that the SLSC beamformer is sensitive to the location of the fiber, which creates an additional PA signal in the transverse SLSC scans that is approximately 20 dB above the dynamic range of the image. In DAS images, the signal due to the fiber is approximately 10 dB below the displayed dynamic range and is therefore not visible in the transverse DAS image of Fig. 8. Lateral resolution seems to improve as the value of M is increased, determined qualitatively by the smaller width of the three seeds in the curvilinear image (top row). The longitudinal scans (bottom row) show better visualization of the seeds with lower values of M.

Performance of the SLSC beamformer as a function of the short-lag value, M, is shown in Fig. 9. Contrast, CNR, and SNR were measured using the longitudinal scans while lateral resolution was measured using seed #3 in the transverse scan. The mean contrast with the SLSC beamformer does not vary by more than 10 dB and is greater than the contrast achieved with DAS beamforming. CNR and SNR generally decrease as M is increased above 2. The CNR in SLSC images is generally greater than CNR in DAS images for lower values of M, while SNR is degraded with the SLSC beamforrmer for all values of M. In addition, the lateral resolution of SLSC images approaches that of DAS images as M is increased and is better than DAS by 0.3 mm when M =10. Although results are only shown for a fiber-sheath tip distance of 3 cm, similar trends were observed for the entire range of varied fiber-sheath tip distances (i.e. 0-5 cm).

A B-mode image of the *ex vivo* tissue implanted with an uncoated brachytherapy seed is shown in Fig. 10(a). The brachytherapy seed is difficult to detect due to the presence of multiple hyperechoic tissue structures. The location of the seed is more clearly visualized in the PA images overlaid on the B-mode images. The SLSC PA image was created with a short-lag value of $M = 5$. The measured contrast, CNR, and SNR were 5.2 dB, 1.8 and 4.0, respectively, in the DAS PA image (Fig. 10(b)) and 29.6 dB, 3.9, and 3.8, respectively, in the SLSC PA image (Fig. 10(c)). Thus, contrast and CNR were improved by 24.4 dB and 2.1, respectively, with the SLSC
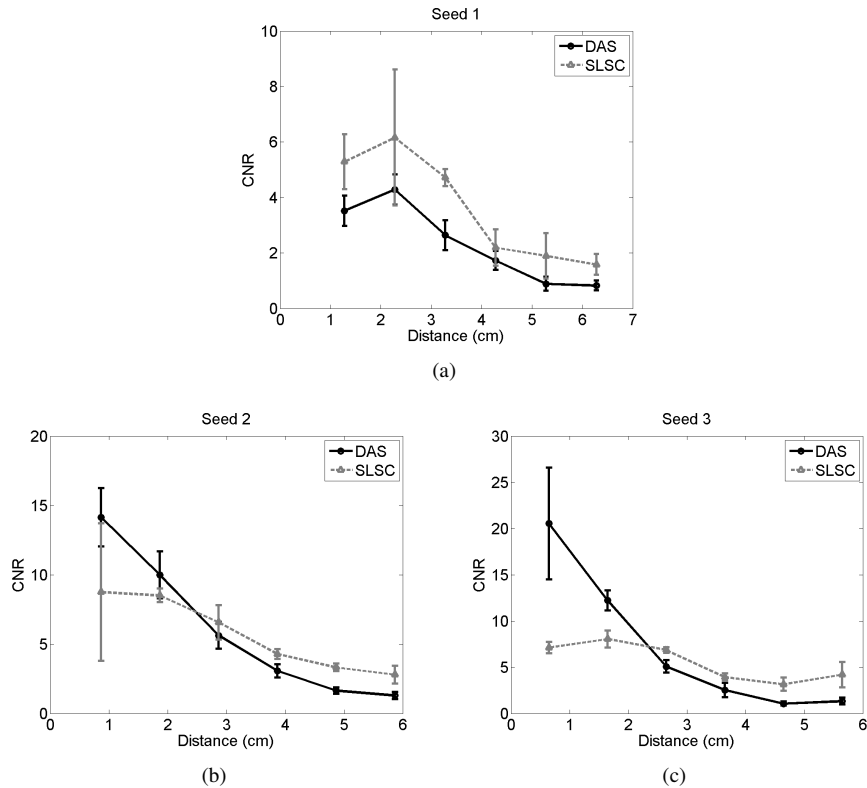
Fig. 7. CNR of seeds #1-3 as a function of distance between the seed and fiber. The SLSC beamformer generally has better CNR for larger fiber-seed distances. Error bars indicate ± one standard deviation of five image frames. SLSC performance metrics were calculated with a short-lag value of *M*=4.

beamformer, while SNR was decreased by 0.2, compared to the DAS image. With increased contrast and CNR and reduced SNR, the SLSC beamformer performs similarly in phantom and *ex vivo* data when compared to the DAS beamformer. Note that the SLSC beamformer increases PA image contrast even in the absence of a coating to increase optical absorption.

4. Discussion

SLSC beamforming is advantageous when applied to PA imaging of structures exposed to minimal local laser fluence. The SLSC beamformer increases signal contrast over a large range of light-target distances when imaging prostate brachytherapy seeds. While these results were obtained with a proposed transperineal light delivery method for photoacoustic imaging of prostate brachytherapy seeds, other light delivery methods, such as transrectal light delivery, may similarly benefit from a coherence-based beamforming approach.

The incident laser beam required for photoacoustic imaging is comparable to ultrasound imaging with a broad, unfocused transmit beam. In this scenario, the spatial coherence of the received signals is mainly determined by the geometry of the target, unlike SLSC applied to pulse-echo ultrasound data acquired with focused transmit beams wherein the spatial coherence of received signals is dually determined by the transmit beam and the target geometry [14, 27]. The SLSC PA image sensitivity to target geometry, and hence sensitivity to seed orientation, is
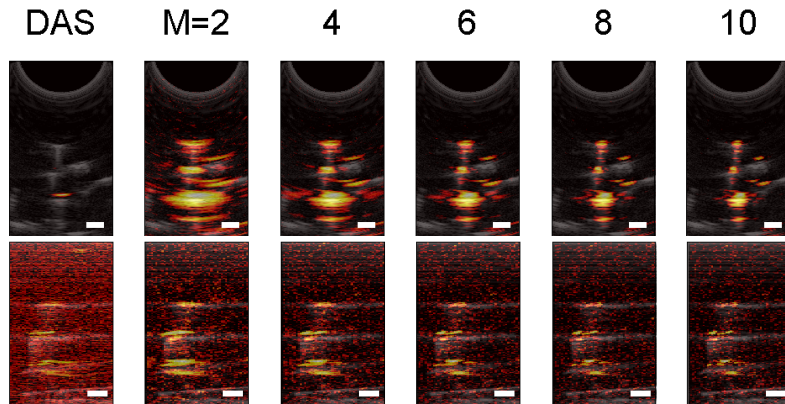
Fig. 8. Transverse (top) and longitudinal (bottom) scans of the three brachytherapy seeds created with the DAS and SLSC beamformers. Short-lag values with the SLSC beamformer are shown for values of M ranging 2-10. The distance between the fiber and sheath tips is 0 cm for the transverse scans and 3 cm for the longitudinal scans. The dynamic range of all PA images is 25 dB. The white bars, each 5 mm in length, denote the image scale. Seed #1 is the uppermost seed in each image.

particularly evident when comparing the transverse and longitudinal scans in Fig. 8.

The SLSC imaging parameter, M, may be adjusted to enhance brachytherapy seed visualization, with the optimal value dependent on factors like seed orientation and the minimum resolution required. When visualizing the long axes of the seeds, lower values of M are preferable because the reduced lateral resolution allows the seed to appear more uniform in the lateral dimension. However, higher values of M are preferred when imaging the diameter of the brachytherapy seeds, as the increased lateral resolution facilitates better localization of the spatially coherent acoustic signals emanating from the point-like source in this orientation.

Calculations of SLSC images are independent of signal amplitude, and thus contrast is relatively constant with the SLSC beamformer as a function of the fiber-seed distance. However, the contrast measurement has large variance, as evident from the largely varying error bars associated with most contrast measurements. These variations are mostly due to the unstable, spatially-incoherent noise regions surrounding the PA signals, as demonstrated in Fig. 4. Random fluctuations in the spatial correlation of the noise regions likely cause the poorer SNR observed with the SLSC beamformer compared to the DAS beamformer.

The apparent trade offs among CNR, SNR, lateral resolution, and M are demonstrated in Fig. 9, where higher values of M offer better lateral resolution at the expense of poorer CNR and SNR. Similar trade offs were observed when the SLSC beamformer was applied to ultrasound data [14, 15, 17]. These trade-offs are associated with changes in spatial frequency content, off-axis spatial coherence information, and background noise sensitivity as the value of M is modulated.

A comparison of *ex vivo* results and phantom measurements obtained at a similar fiber-seed distance of 6 mm (see Fig. 6) indicates that contrast and SNR in DAS images were decreased by 19-25 dB and factors of 4-8, respectively, in the *ex vivo* experiment with an uncoated seed. These decreases may be partially due to the greater optical and acoustic scattering with the *ex vivo* tissue or the factor of 1.4 decrease in energy density in the *ex vivo* experiment. Otherwise, the decreases are due to the lack of an absorption-enhancing coating, which would be consistent with the findings of Pan et al. [9].
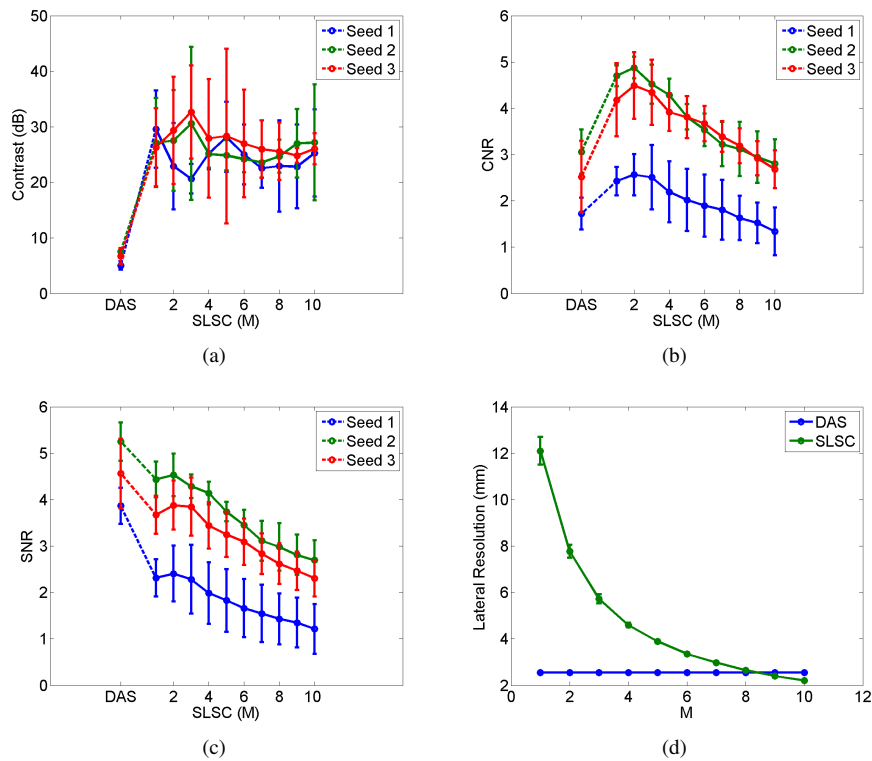
Fig. 9. (a) Contrast, (b) CNR, and (c) SNR as a function of the short-lag value, M, calculated at a fiber-sheath tip distance of 3 cm. (d) Lateral resolution in DAS and SLSC photoacoustic images was measured using seed #3 and the curvilinear probe. Error bars indicate ± one standard deviation of five image frames.

Similar improvements with SLSC imaging were prevalent regardless of the use of ink coating. Thus, the application of a coating to increase optical absorption is not a requirement for improved contrast with the SLSC beamformer. Results suggest that this beamforming approach may be combined with various contrast-enhancing seed alteration approaches [9, 10] to further improve seed visualization in photoacoustic images.

One limitation of this study is that the energy density in the phantom and *ex vivo* experiments exceeded the ANSI limit for human exposure [22]. In future implementations, energy density may be decreased with a custom-built sheath tip that has a larger surface area. Even with this type of modification, a lower energy might still be required to satisfy the ANSI limit. In this case, the greater contrast, CNR, and SNR measured with the DAS beamformer at the shorter light-target distances would likely not be achievable when imaging brachytherapy patients. Instead, the poorer CNR, SNR, and contrast values measured with the DAS beamformer at the larger fiber-seed distances are more likely, as these seeds were exposed to less light fluence and lower energy densities. These poorer values are likely more representative of the challenges expected during clinical implementation. Seed visualization and the quantitative performance metrics at these larger distances were improved with the SLSC beamformer. Thus, this coherence-based beamforming approach appears to be more promising than conventional DAS beamforming for *in vivo* photoacoustic imaging of prostate brachytherapy seeds within the ANSI limit.
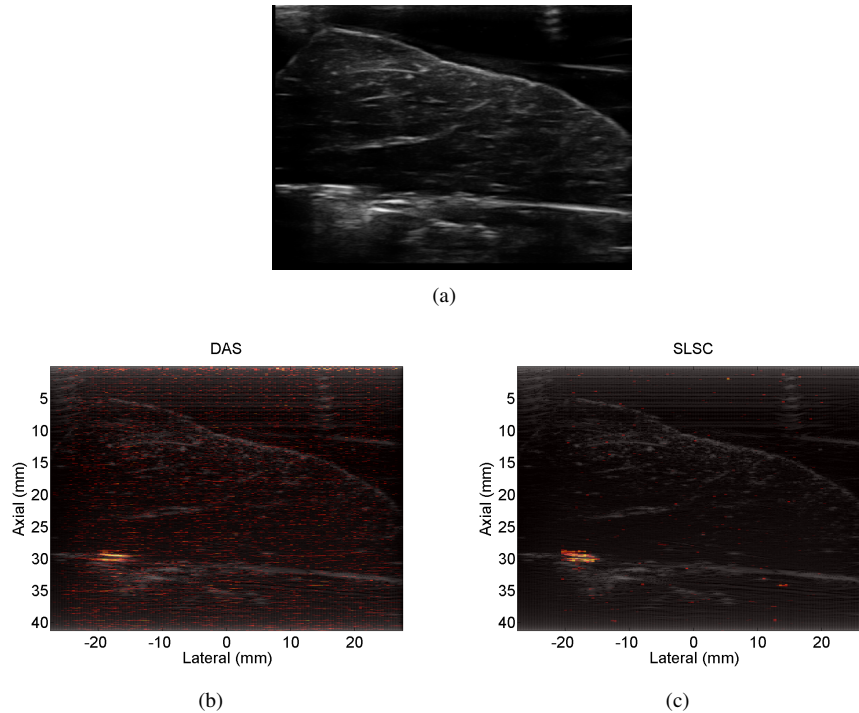
Fig. 10. (a) B-mode image of the *ex vivo* bovine liver implanted with an uncoated brachytherapy seed, acquired with the linear array of transrectal probe. Photoacoustic (PA) images created with (b) DAS and (c) SLSC beamformers were overlaid on the ultrasound image and shown with 10 dB dynamic range.

5. Conclusion

SLSC beamforming of photoacoustic data has benefits for detecting brachytherapy seeds intra-operatively. The method was demonstrated using a transrectal ultrasound probe, an optical fiber for proposed transperineal interstitial light delivery to the prostate, and a needle template for seed insertion parallel to the longitudinal axes of the fiber and probe. The method was also validated with *ex vivo* tissue. While amplitude-dependent beamformers like the DAS method have diminishing contrast with increasing distance from the light source, the SLSC beamformer has relatively constant contrast over the same range of distances and is demonstrated as a preferred beamformer for photoacoustic imaging of structures exposed to minimal local laser fluence.

Acknowledgments